# Statics, linear, and nonlinear dynamics of entangled polystyrene melts simulated through the primitive chain network model

Takatoshi Yaoita,[1,a)] Takeharu Isaki,[1] Yuichi Masubuchi,[2] Hiroshi Watanabe,[2] Giovanni Ianniruberto,[3] Francesco Greco,[4] and Giuseppe Marrucci[3]
[1]*Material Science Laboratory, Mitsui Chemicals, Inc., Chiba 299-0265, Japan*
[2]*Institute for Chemical Research, Kyoto University, Kyoto 611-0011, Japan*
[3]*Dipartimento di Ingegneria Chimica, Università "Federico II", P.le Tecchio 80, 80125 Napoli, Italy*
[4]*Istituto di Ricerche sulla Combustione, CNR, P.le Tecchio 80, 80125 Napoli, Italy*

(Received 5 December 2007; accepted 27 February 2008; published online 15 April 2008)

Simulation results of the primitive chain network (PCN) model for entangled polymers are compared here to existing data of diffusion coefficient, linear and nonlinear shear and elongational rheology of monodisperse polystyrene melts. Since the plateau modulus of polystyrene is well known from the literature, the quantitative comparison between the whole set of data and simulations only requires a single adjustable parameter, namely, a basic time. The latter, however, must be consistent with the known rheology of unentangled polystyrene melts, i.e., with Rouse behavior, and is therefore not really an adjustable parameter. The PCN model adopted here is a refined version of the original model, incorporating among other things a more accurate description of chain end dynamics as well as finite extensibility effects. In the new version, we find good agreement with linear rheology, virtually without adjustable parameters. It is also shown that, at equilibrium, Gaussian statistics are well obeyed in the simulated network. In the nonlinear range, excellent agreement with data is found in shear, whereas discrepancies and possible inadequacies of the model emerge in fast uniaxial elongational flows, even when accounting for finite extensibility of the network strands. © *2008 American Institute of Physics*. [DOI: 10.1063/1.2899653]

## I. INTRODUCTION

It is known that the dynamics of entangled polymers is complex, simultaneously including many mechanisms such as reptation, tube-length fluctuations, constraint renewal, both thermal and convective, and chain stretch. Because of such complexity, analytical theories are conveniently replaced by molecular simulations, provided that the latter are suitably coarse grained so as to encompass the large relaxation times of such systems.

A convenient coarse graining can use as basic unit the subchain between consecutive entanglements so that the polymer chain is, in fact, replaced by the so-called primitive chain, first introduced by Doi and Edwards.[1] With such coarse graining, entanglements can be depicted as sliplinks through which the chain slides in its longitudinal motion. Simulations based on this picture were originally proposed by Hua and Schieber,[2] Doi and Takimoto,[3] Masubuchi *et al.*,[4] the latter is the only simulation of this kind that considers an actual network in a three-dimensional (3D) box with periodic boundary conditions, similarly to atomistic simulations. For such to be the case, sliplinks are used to connect chains in pair, thus creating the network.

With respect to previous reports on the primitive chain network (PCN) model, we present here a revised version that accounts more accurately for the following aspects: (i) Hooking events of chain ends upon neighboring chains (sliplink creation) here occur in a way that maintains equilibrium of chain ends, differently from the previous version where some artificial chain stretch was introduced upon hooking. (ii) The friction is here attributed to subchains accounting for the variable number of monomers they contain. In the previous version, sliplinks had a fixed friction, which does not seem suitable for nonequilibrium situations where the number of entanglements (hence of sliplinks) is expected to change. (iii) The incompressibility constraint is here enforced with a simpler quadratic mean-field potential. (iv) Account is taken for finite extensibility effects, i.e., for non-Gaussian behavior of the network strands. This change is believed to be necessary to deal with nonlinear response in fast flows.

With the new code, we have simulated both the static and the dynamic responses of monodisperse linear polymers (although the extension to a known polydispersity is straightforward) and compared them to a consistent set of linear and nonlinear data of polystyrene melts reported in the literature.[5,6] It should be emphasized that since all basic properties of polystyrene melts, including the plateau modulus, are well established, our simulations have no adjustable parameters except for a basic characteristic time, representative of the basic friction at a reference temperature. The latter must anyhow be consistent with existing data on Rouse behavior in unentangled melts.

Accordingly, the paper is organized as follows. First, the model is synthetically presented, emphasizing the changes with respect to previous versions. After checking that the

[a)]Author to whom correspondence should be addressed. Tel: +81-438-64-2320. FAX: +81-438-64-2378. Electronic mail: takatoshi.yaoita@mitsui-chem.co.jp.

 

statics obeys Gaussian statistics, and that relaxation times and self-diffusion coefficients display the correct scalings with the polymer molar mass, the results of simulations in both the linear and the nonlinear ranges are compared to existing data.

## II. MODEL

In the PCN model, polymer chains are coarse grained at the level of the entanglement molecular weight, thus becoming similar to the primitive chains of tube theory. In other words, each polymer chain is replaced by a sequence of subchains connecting consecutive entanglements. The entanglements themselves are modeled as sliplinks, i.e., small rings through which monomers can slide from one subchain to the next along the same chain. Sliplinks are assumed to join chains in pairs (binary topological interaction). Because of such connectivity among different chains, the system forms a 3D physical network, with tetrafunctional nodes (the sliplinks) and pendent chain ends. Dynamics of the network results from node (and chain-end bead) motion in space, monomer transport through sliplinks, and creation/destruction of sliplinks, induced by hooking/unhooking processes between chains. The simulation of such dynamics is carried on in a box (with periodic boundary conditions), typically containing some $10^4$ subchains (and sliplinks).

### A. 3D motion of nodes

Time evolution of the position $\mathbf{R}$ of each sliplink obeys the following 3D Langevin (force balance) equation, where inertia is ignored,

$$\zeta(\dot{\mathbf{R}} - \boldsymbol{\kappa}\cdot\mathbf{R}) = \sum_i^4 \mathbf{F}_i + \mathbf{F}_B + \mathbf{F}_f. \tag{1}$$

The left-hand side of Eq. (1) is the node friction force, with $\dot{\mathbf{R}}$ as the time derivative of $\mathbf{R}$, tensor $\boldsymbol{\kappa}$ as the externally imposed velocity gradient, and $\zeta$ as the friction coefficient associated with the node, accounting for the four (half) subchains emanating from the node,

$$\zeta = \zeta_m \sum_i^4 n_i/2. \tag{2}$$

In Eq. (2), $\zeta_m$ is the friction coefficient of a monomer (Kuhn segment) and $n_i$ is the current number of monomers in the $i$th subchain.

The right-hand side of Eq. (1) includes all other forces acting on the node, namely, the elastic forces $\mathbf{F}_i$ from the four subchains converging into the node, the Brownian force $\mathbf{F}_B$ of thermal origin, linked to $\zeta$ by the fluctuation-dissipation theorem, and a field force $\mathbf{F}_f$ which, for the homopolymer case, is representative only of the incompressibility constraint, i.e., it opposes clustering of the nodes.

The elastic force $\mathbf{F}$ has the classical expression used for (phantom) entropic springs. Also accounting for finite extensibility effects, we write

$$\mathbf{F} = \frac{3kT}{nb^2} f(r)\mathbf{r}, \tag{3}$$

with $kT$ as the thermal energy, $b$ as the Kuhn monomer length, $\mathbf{r}$ as the subchain end-to-end vector, and $f(r)$ as a non-Gaussian correction, which is unity for Gaussian chains, and diverges at the maximum extension $r_{\max}=nb$ of the subchain. We use the Padé approximation[7] of the inverse Langevin function,

$$f(r) = \frac{1 - r^2/3r_{\max}^2}{1 - r^2/r_{\max}^2}. \tag{4}$$

In many simulations where stretching of the chains is not expected, $f(r)$ is directly set to unity (Gaussian simulations).

The Brownian force $\mathbf{F}_B$ is a random force with zero mean value and variance given by ($\mathbf{I}$ is the unit tensor)

$$\langle \mathbf{F}_B(t)\mathbf{F}_B(t')\rangle = 2kT\zeta\delta(t-t')\mathbf{I}. \tag{5}$$

As previously mentioned, the field force $\mathbf{F}_f$ is introduced to somehow account for excluded volume effects in the PCN model, where subchains are phantom, with the aim of smoothing possible density inhomogeneities. We assume a free energy $A$ per unit volume related to the fluctuating concentration $N$ of nodes and obtain the force from the chemical potential $\mu = \partial A/\partial N$ as

$$\mathbf{F}_f = -\nabla\mu. \tag{6}$$

In this paper, a simple one-parameter quadratic free energy $A$ is adopted,

$$\frac{A}{kT} = \alpha\langle N\rangle\left(1 - \frac{N}{\langle N\rangle}\right)^2, \quad \frac{\mu}{kT} = 2\alpha\frac{N}{\langle N\rangle} + \text{const}, \tag{7}$$

where $\langle N\rangle$ is the average node concentration in the simulation box. Both $\langle N\rangle$ and $N$ are dynamic variables; the latter are determined by counting sliplinks locally in a sub-box. Consistently with the coarse-graining adopted, which is at the scale of the equilibrium mean distance $a$ between consecutive sliplinks, sub-boxes are taken of volume $a^3$, typically containing some ten subchains. Gradients in chemical potential are evaluated from differences between neighboring sub-boxes.

Concerning chain end beads, their dynamics is still described by Eq. (1), but of course with a single elastic force (no sum), and with a coefficient $\zeta$ accounting for the friction of half the terminal subchain only.

### B. 1D monomer sliding through nodes

The rate of sliding of monomers from one subchain to the next through the sliplink is described through the following one-dimensional (1D) Langevin equation:

$$\zeta_s\frac{\dot{n}}{\rho_m} = (F_i - F_{i-1}) + f_B + f_f, \tag{8}$$

where $\dot{n}$ is the rate of change of monomers in subchain $i$ due to monomer exchange to or from the adjacent subchain $i-1$ and $\rho_m$ is the linear density of monomers, $n/r$, in the subchain (either $i$ or $i-1$) that looses monomers.

The sliding-friction coefficient $\zeta_s$ in Eq. (8) accounts for the friction of the two adjacent half-subchains involved in the local sliding process,

$$\zeta_s = \zeta_m \frac{n_i + n_{i-1}}{2}. \tag{9}$$

The Brownian force $f_B$ is a 1D random force with zero mean, obeying

$$\langle f_B(t) f_B(t') \rangle = 2kT\zeta_s \delta(t - t'). \tag{10}$$

Finally, $f_f$ is the field force, calculated as one-half the gradient of $\mu$ along the chain. The $\frac{1}{2}$ factor is due to the fact that, on average, the monomers involved in a sliding event are one-half those associated to node motion.

It is fair to note that the choice of a variable friction in the subchains in proportion to the monomers they contain (hence, maintaining a constant friction in the whole chain) was also made in the recent works by Schieber and co-workers.[8,9]

### C. Renewal of entanglements

Sliplinks are created and removed through chain ends hooking and unhooking neighboring chains. Such processes are controlled by the number of monomers in the chain ends: A new entanglement is created if the end subchain has many monomers, whereas the end entanglement of a chain is removed if the chain end has less than a minimum monomer number. The monomer number "window" outside of which these "topological events" occur has been taken as $0.5n_0 < n < 1.5n_0$, with $n_0$ as the number of monomers in any subchain at network creation (see below) and, in fact, equal to the average number of monomers in a subchain under equilibrium conditions. The value of $n$ in the chain ends is checked with a frequency dictated by the relaxation time $\tau_{\text{end}}$ of chain ends themselves, assumed to be equal to the Rouse time of a tethered chain with $n_0$ monomers, i.e., $\tau_{\text{end}} = 4n_0^2 b^2 \zeta_m / 3\pi^2 kT$.

Figures 1 reports the geometrical details of how the hooking event is handled in the new code. Figure 1(a) shows how the selection of the partner is made, namely, by choosing randomly among all subchains intercepting the sphere of radius $a = b\sqrt{n_0}$ (root-mean-square equilibrium distance between entanglements), centered at the sliplink next to the hooking chain end. The new sliplink is then located at the single interception point, or at anyone of the two in case of double interception. Figure 1(b) shows an example where the choice was for a subchain with a single interception. Of the $n > 1.5n_0$ monomers belonging to the hooking chain end, $n_0$ are assigned to the new subchain, while $n - n_0$ remain in the new shortened chain end. Finally, the new end bead is located randomly at a distance $b\sqrt{n - n_0}$ from the new sliplink. It is worth noting that, by these rules, the two new segments are both at equilibrium. In the subchain which has been hooked, and hence divided in two segments by the new sliplink, monomers are split in proportion to their respective lengths. Notice that these rules use average values, thus ignoring fluctuations in both distance and monomer number. However, in a few time steps, the Langevin equations soon restore fluctuations in the subchains involved. Finally, it is worth mentioning that, throughout the simulation algorithm, we impose that the monomer number in a subchain never goes below $n = 1$. Hence, if in splitting monomers between subchains one of them is so short as to receive less than one monomer, $n = 1$ is in fact assigned to it.

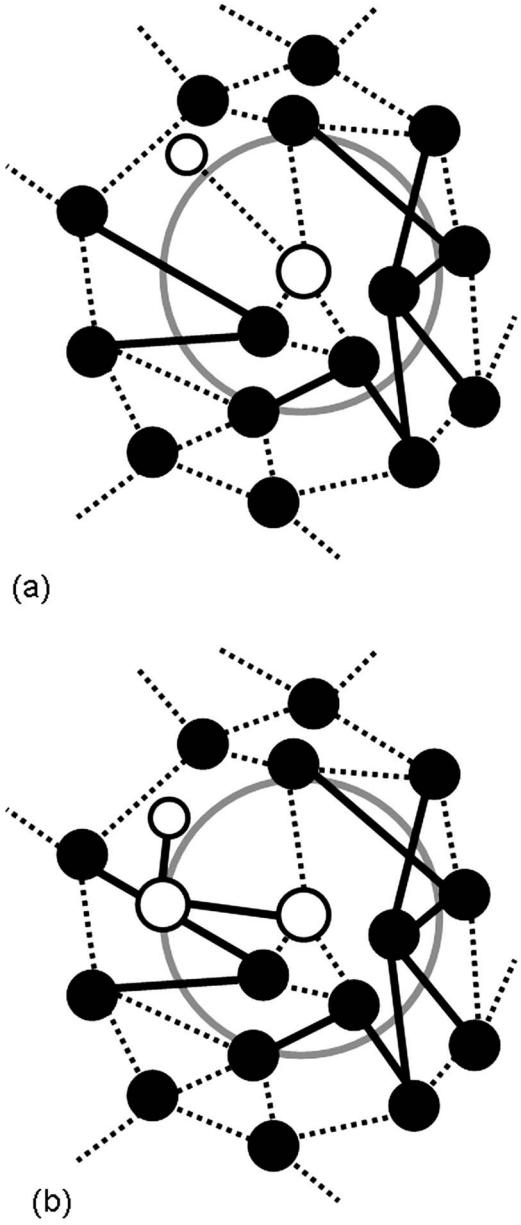


FIG. 1. Schematic illustration of the hooking process as modified in this work. (a) The partner is searched by using a sphere of radius $a$ (the circle in the figure). The center of the sphere is located at the last sliplink (large open circle), from which the searching chain end emanates (small open circle). Possible partners are the subchains intersecting the sphere (solid segments). All other subchains are indicated as dashed segments. (b) One of the possible partners has been randomly selected, and the new sliplink has been created on the surface of the sphere (second large open circle). Monomers are distributed as described in the text. The chain end is randomly repositioned (small open circle) with an equilibrium length.

The unhooking event ($n < 0.5n_0$) is dealt with in a way essentially equivalent to the previous version of the PCN model.[4] The sliplink next to the unhooking chain end is removed, and both the unhooking chain and the partner chain

are straightened, i.e., in both chains the two subchains attached to the removed sliplink collapse into one.

### D. Simulation parameters

The Langevin equations previously written are made nondimensional by using as unit of length the distance $a$ between sliplinks, as unit of energy $kT$ and as unit of time the grouping $\tau=n_0^2b^2\zeta_m/3kT$. Finally, the monomer number $n$ is conveniently normalized by taking the ratio to $n_0$. All such choices are made with the purpose of simplifying as much as possible the nondimensional form of the equations. It is worth noting that the unit of time does not coincide with the time interval for topological changes (hooking and unhooking events). The latter, in nondimensional units becomes $\tau_{\mathrm{end}}/\tau=4/\pi^2\cong 0.4$.

The nondimensional equations thus obtained only contain the free energy parameter $\alpha$. Its value was fixed at 2.0, a value which appears sufficient to avoid unphysical clustering of the nodes of the primitive chain network. Larger values of $\alpha$ have also been used, without significant changes in the simulation results. Hence, no parameters in fact appear in the nondimensional dynamical equations.

Parameters of the model do appear, however, in the preparation of the simulation box. Quite apart from the chosen chain architecture (linear, star, H shaped, etc.) and limiting our present discussion to linear chains only, the parameters are the numbers of subchains constituting the chains of a polydisperse sample, reducing to a single parameter $Z$ for the monodisperse situation ($Z-1$ is the number of entanglements per chain). When the box is created, the same monomer number $n_0$ is assigned to each subchain ($\tilde{n}=1$, in normalized units). As a consequence of dynamics, however, the system will equilibrate, and all dynamic variables will therefore fluctuate, including the number $Z$ of subchains, the latter because of network rearrangement initiated by chain ends. Hence, even for a monodisperse sample under equilibrium conditions, $Z$ becomes somewhat distributed, and the average $\langle Z\rangle$ can come out slightly different from the preset initial value $Z_0$. Needless to say, for any given chemistry, $Z_0$ is proportional to the molar mass $M$ of the polymer.

Another parameter of the simulation is the subchain density $\nu$ (and consequently the node density $\langle N\rangle$) with which we fill the box. It so turns out, however, that such a density is not a relevant parameter in our simulations insofar as, all other conditions being the same, the stress tensor is proportional to $\nu$. We adopted a fixed value of 10 subchain in the volume $a^3$ (our unit volume), as is typical of most polymer melts, and which guarantees that hooking processes are successful.

In conclusion, and limiting our discussion to linear chains only, the single constitutive parameter of the simulations is the number $Z_0$ of subchains per chain (or its distribution in the polydisperse case).

We now consider how the nondimensional results of the simulations are compared to data, specifically to rheological data, and which dimensional parameters are required for such a comparison. To this end, we note that the stress tensor $\mathbf{T}$ in the network of (phantom) subchains contained in the box is calculated as

$$\mathbf{T}=\frac{\Sigma\mathbf{F}\mathbf{r}}{V_{\mathrm{box}}}=\nu\frac{\Sigma\mathbf{F}\mathbf{r}}{N_{\mathrm{subchain}}}=\nu kT\frac{\Sigma\tilde{\mathbf{F}}\tilde{\mathbf{r}}}{N_{\mathrm{subchain}}}=\nu kT\tilde{\mathbf{T}}, \tag{11}$$

where $\mathbf{r}$ is the subchain end-to-end vector, $\mathbf{F}$ is the corresponding elastic force, the tilde indicates nondimensional quantities, and the sum extends over all subchains in the box of volume $V_{\mathrm{box}}$. Notice that no contribution from the density-preserving field forces $\mathbf{F}_f$ is included in Eq. (11). Indeed, we have verified that the contribution of the field forces to the stress tensor remains isotropic in all conditions examined. In Eq. (11), with the symbol $N_{\mathrm{subchain}}=\nu V_{\mathrm{box}}$, we indicate the number of subchain originally put in the box. Finally, the fraction appearing in the next to last expression of Eq. (11) is the nondimensional stress tensor $\tilde{\mathbf{T}}$ as calculated in the simulations. It so appears that in order to compare simulations to data, we need to specify the modulus

$$G=\nu kT=\frac{\rho RT}{M_{\mathrm{subchain}}}, \tag{12}$$

where $\rho$ is polymer density, $R$ is the gas constant, and $M_{\mathrm{subchain}}$ is the molar mass of the subchains (as initially placed in the simulation box). It is worth emphasizing that $\tilde{\mathbf{T}}$ is independent of the subchain density used in the simulation box since both the sum in the numerator of the fraction defining $\tilde{\mathbf{T}}$ and $N_{\mathrm{subchain}}$ are proportional to the subchain density. Hence, the value of $\nu$ appearing in Eq. (12) does not refer to the arbitrary value of the subchain density used in the simulation. Rather, it refers to the subchain density of the experimental sample to be compared to the simulation results.

Equation (12) superficially resembles the expression for the plateau (or rubber-elasticity) modulus $G_N^{(0)}$, as given for example by Ferry,[10]

$$G_N^{(0)}=\frac{\rho RT}{M_e^F}. \tag{13}$$

We recall, however, that Eq. (13) defines the entanglement molecular weight $M_e^F$ based on the assumption of affine deformation of entangled networks, i.e., by ignoring both the 3D Brownian fluctuations of the network modes and the longitudinal monomer sliding across entanglements. The effect of monomer sliding is explicitly accounted for in the tube model of Doi and Edwards, resulting in a $\frac{4}{5}$ factor which affects either the modulus or, equivalently, the entanglement molecular weight definition, which becomes $M_e=\left(\frac{4}{5}\right)M_e^F$.[1] The Brownian fluctuation of the network nodes, already relevant in rubbers, gives rise to another factor of $\frac{1}{2}$ with respect to the affine modulus.[11] Now, since our simulations include both node fluctuation and monomer sliding, we expect that the following relationship holds true:

$$G_N^{(0)}=\frac{1}{2}\frac{4}{5}\frac{\rho RT}{M_{\mathrm{subchain}}}=0.4\frac{\rho RT}{M_{\mathrm{subchain}}}, \tag{14}$$

which implies

$$M_{\text{subchain}} = 0.4 M_e^F. \tag{15}$$

A relationship similar to Eq. (14) was already suggested in previous reports of our simulations, where relaxation after a step strain in the linear range was investigated.[12] The simulations in Ref. 12 show that in a short time after application of the strain, a plateau is reached which falls close to one-half the initial stress. It is further noted that also some recent atomistic simulations of the primitive path have shown a molar mass between consecutive entanglements close to 0.4 times the classical Ferry value.[13]

By using Eq. (15), $M_{\text{subchain}}$ can be derived from well established values of $M_e^F$ (or equivalently of $G_N^{(0)}$), as reported in the literature for most polymer melts.[10] From the known values of polymer density, the parameter $G$ is then calculated from Eq. (12). Hence, in our simulations, $G$ *cannot* be considered as an adjustable parameter.

Furthermore, we can obviously write

$$Z_0 = M/M_{\text{subchain}}, \tag{16}$$

where $M$ is the molar mass of the whole chain. Hence, if $M$ is known, also the value of $Z_0$ to be used in the simulation is *not* an adjustable parameter.

In conclusion, the *single adjustable parameter* needed to compare simulations to data, which (temporarily) is not anticipated by arguments of model self-consistency, is the characteristic time $\tau$ (but see next section). We recall that $\tau$ is a local quantity, related to the subchain rather than the whole chain, and is therefore independent of chain architecture and molar mass. It only varies with varying either the polymer chemistry or the temperature. The latter dependence typically obeys the Williams-Landel-Ferry (WLF) time-temperature equation, the parameters of which are well known for most polymers.[10] Hence, if $\tau$ has been determined at one temperature, the model becomes fully predictive at any other temperature.

## III. RESULTS AND DISCUSSION

The organization of this section is as follows. First, we check the equilibrium statistics of both chains and subchains obtained from simulations against the classical predictions of Gaussian theory. No parameter is required at this stage. We then compare simulation results for $G'$ and $G''$ with some existing experimental data of nearly monodisperse polystyrene melts by using constitutive parameters reported in the literature plus a single adjustable parameter, namely, the basic time $\tau$. Next, we successfully check the value of $\tau$ against zero-shear viscosity data of unentangled polystyrene melts by using the Rouse theory and further compare simulation results of entangled melt zero-shear viscosity and center-of-mass diffusion coefficient to existing data. Finally, we extend the comparison to the nonlinear range, both in shear and in uniaxial elongational flows, without additional parameters. In the results shown in the following the simulation box is $8 \times 8 \times 8$ unless differently specified.

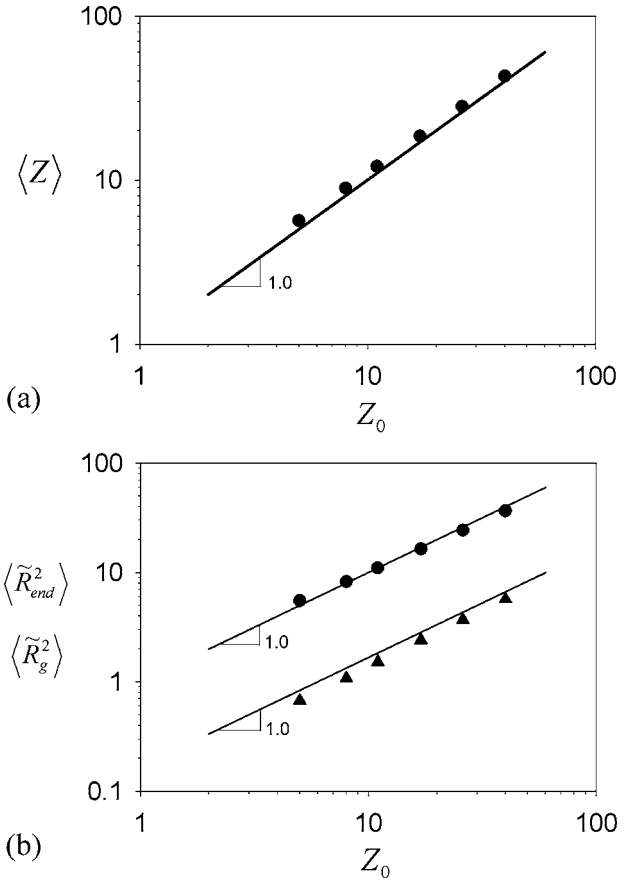


FIG. 2. Equilibrium properties of the chains as a function of the subchain number $Z_0$: (a) average number of subchains $\langle Z \rangle$ after equilibration, (b) nondimensional average square end-to-end distance $\langle \tilde{R}^2_{\text{end}} \rangle$ (circles), and nondimensional average square radius of gyration $\langle \tilde{R}^2_g \rangle$ (triangles). The lines indicate the corresponding prediction for Gaussian chains.

### A. Basic chain and network properties

Figure 2(a) shows the mean number $\langle Z \rangle$ of subchains per chain after equilibration as a function of the initial value $Z_0$. Good agreement between the two indicates that the dynamical rules, specifically the hooking/unhooking dynamics, essentially fulfill detailed balance. Figure 2(b) reports the mean square end-to-end distance of the chain $\langle \tilde{R}^2_{\text{end}} \rangle$ and the mean square radius of gyration $\langle \tilde{R}^2_g \rangle$ as a function of $Z_0$, lines indicating the corresponding Gaussian chain results. Simulations in Fig. 2(b) are in reasonable agreement with the Gaussian predictions, especially for longer chains. Short chains probably suffer somewhat of short-range correlations induced by force balance at the entanglements as portrayed in the model. Results in Fig. 2(b) improve significantly over previous reports.[4]

Figure 3 shows, on the left axis, the nondimensional longest relaxation time $\tilde{\tau}_d$ as a function of $Z_0$, obtained by monitoring (similar to previous simulations[4]) the autocorrelation function of the end-to-end vector at equilibrium. The solid line in Fig. 3 is the prediction of pure reptation: $\tilde{\tau}_d = 3Z_0^3/\pi^2$. Due to tube length fluctuations and possibly constraint release, $\tilde{\tau}_d$ is known to fall below the reptation prediction, approaching pure reptation progressively, as $Z_0$ in-

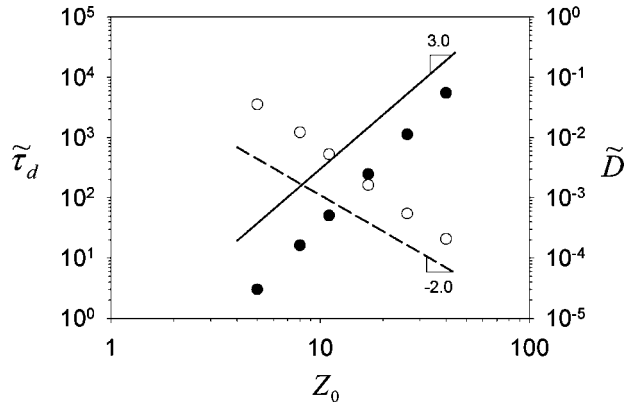


FIG. 3. Dependence on $Z_0$ of the nondimensional longest relaxation time $\tilde{\tau}_d$ (closed circles, left axis) and of the nondimensional self-diffusion coefficient $\tilde{D}$ (open circles, right axis). The solid and dashed lines are predictions of pure reptation theory.

creases. Simulations indeed show such behavior; the data in Fig. 3 are well fitted by $\tilde{\tau}_d \propto Z_0^{3.5}$, in agreement with the typical power-law scaling.[1,14]

On the right axis of Fig. 3, we report the nondimensional self-diffusion coefficient $\tilde{D}$ obtained by monitoring the displacement of the center of mass of the chains during equilibrium simulations. The theoretical line based on pure reptation is given by $\tilde{D}=1/(9Z_0^2)$ (dashed line in Fig. 3). Due to the additional dynamic mechanisms, $\tilde{D}$ is expected to be larger, as indeed found by the simulations. Our results for $\tilde{D}$ can be fitted by the power law $\tilde{D} \propto Z_0^{-2.5}$, not too different from the experimental scaling $Z_0^{-2.3\pm0.1}$, as reported by Lodge.[15] Notice that, although the exponents for $\tilde{\tau}_d$ and $\tilde{D}$ from the simulations are slightly larger than usually reported, the product $\tilde{\tau}_d\tilde{D}$ comes out to scale with the first power of $M$.

Figure 4 shows the statistics of the subchains (or primitive chain segments) as a function of $Z_0$. The mean subchain length $\langle \tilde{r} \rangle$ shown in Fig. 4(a) turns out somewhat smaller than our unit length, consistently with the existence of a dispersion, and with the fact that the mean square segment length $\langle \tilde{r}^2 \rangle$ shown in Fig. 4(b) is close to unity. The latter result agrees with the statistics of the whole chain, which are close to the equilibrium Gaussian (see Fig. 2). Finally, Fig. 4(c) shows the mean ratio $\langle \tilde{r}^2/\tilde{n} \rangle$ between the square subchain length and the monomer number, which is an index of how close to Gaussian behavior the subchain itself is. The Gaussian subchain at equilibrium should have $\langle \tilde{r}^2/\tilde{n} \rangle = 1$, as indeed shown in Fig. 4(c), whereas with the previous hooking scheme, we had $\langle \tilde{r}^2/\tilde{n} \rangle \simeq 1.25$, showing that stretch of the chain ends due to the previous hooking rule propagated throughout the chain. In all results considered so far (Figs. 2–4), the error bars are not reported because they are smaller than the symbol size.

### B. Linear viscoelasticity

We here compare our simulation results with some existing linear viscoelastic data on nearly monodisperse melts, as listed in Table I. We have chosen those systems, actually only polystyrenes, for which nonlinear results for shear

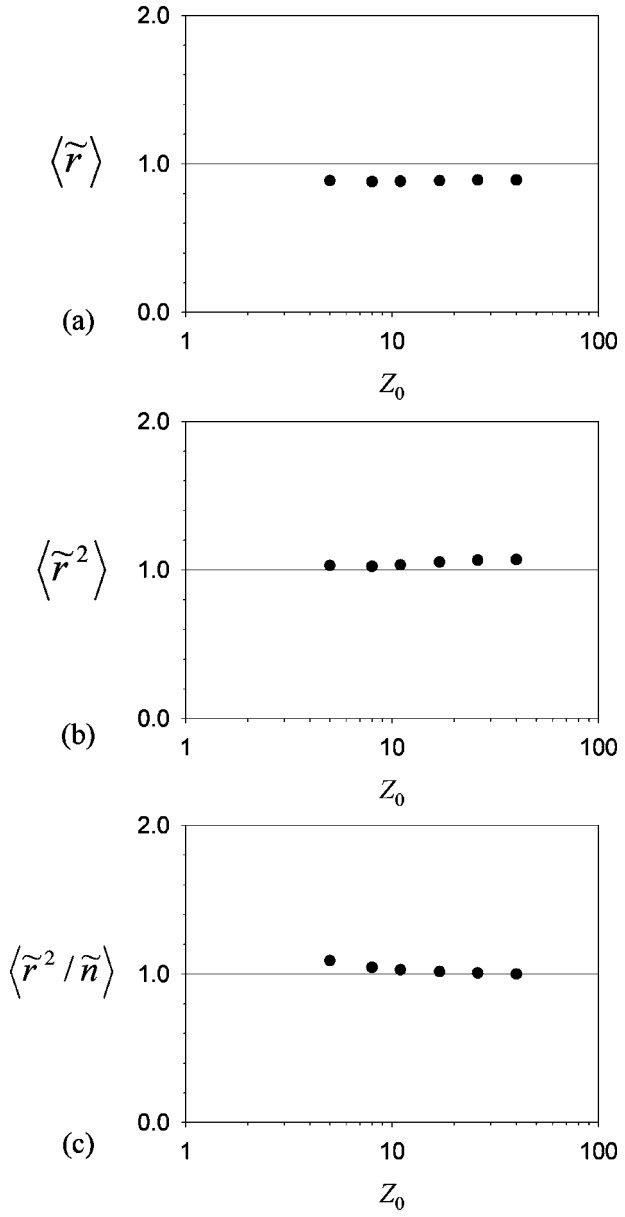


FIG. 4. Equilibrium properties of the subchains as a function of $Z_0$: (a) average length, (b) average square length, and (c) average of the ratio $\tilde{r}^2/\tilde{n}$.

and/or elongational flows are also available. For polystyrene melts, $M_e^F$ appears to be essentially temperature independent. We have chosen the value $M_e^F = 18\,000$, as reported by various authors.[10,16] Hence, Eq. (15) gives $M_{\text{subchain}} = 7200$, from which we obtain the values of $Z_0$ reported in Table I to be used in the simulations. The simulation results for $G'$ and $G''$ were obtained by actually oscillating with a small amplitude the simulation box for several cycles and by fitting the stress

TABLE I. Polystyrene melts considered in this work (Refs. 5 and 6) and the corresponding values of $Z_0$ used in the simulations, as derived from Eqs. (15) and (16).

| Sample | $M_w$ (kg/mol) | $M_w/M_n$ | $T$ (°C) | $Z_0$ |
|---|---|---|---|---|
| PS200k | 200 | 1.04 | 130 | 28 |
| PS390k | 390 | 1.06 | 130 | 54 |
| PS200k-S | 200 | 1.06 | 175 | 28 |

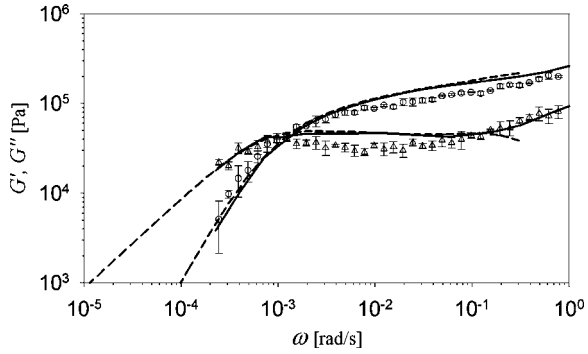


FIG. 5. Viscoelastic moduli $G'$ and $G''$ as a function of frequency. The curves are data for PS200k (solid lines) and for PS200k-S (dashed lines) from Refs. 5 and 6. Symbols with error bars are simulation predictions.

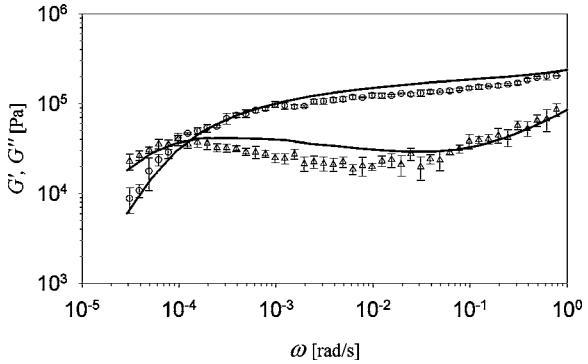


FIG. 6. Viscoelastic moduli at higher molar mass. The curves are data for PS390k from Ref. 5 and symbols are simulation predictions.

in each cycle (except the first) with a sine function. From those functions, average values of moduli, and error bars, were calculated.

The curves in Fig. 5 are $G'$ and $G''$ data for PS200k and PS200k-S, taken at different temperatures of 130 and 175 °C, respectively. The data at higher temperature were shifted in Fig. 5 both vertically (by a factor of 0.92) to account for the effect of temperature on $\rho T$ (data for $\rho$ taken from Ref. 17) and horizontally (by a factor of $0.91\times10^{-3}$) according to the WLF equation: $\log a_T=-c_1^0(T-T_0)/[c_2^0+(T-T_0)]$, where $c_1^0=8.86$, $c_2^0=101.6K$, $T_0=136.5$ °C, and $T$ is in °C.[6] Superposition of the two sets of data is certainly satisfactory.

The simulation results reported in Fig. 5 are also obtained by shifting the nondimensional results (for $Z_0=28$) both vertically and horizontally. The vertical shift $G$ at 130 °C is calculated from Eq. (12) as $G=0.47$ MPa. The horizontal shift $\tau$ is the single fitting parameter in this figure, and we have set (at $T=130$ °C) $\tau=1.3$ s. The simulation results reported in Fig. 5 show good agreement with data, except perhaps in the intermediate region of frequency where the simulated moduli, particularly $G''$, fall somewhat lower than data. Notice, however, that while chains are exactly monodisperse in simulations, data refer to samples with some polydispersity (see Table I).

The parameter $\tau$, just as the shift factor $a_T$, is very sensitive to temperature. As a first check on the value used here, we compare this basic time to that reported in Ref. 18, which refers to $T=169.5$ °C. By applying the WLF equation reported above, we obtain $\tau=2.15\times10^{-3}$ s at $T=169.5$ °C. This value nicely compares with that reported by Likhtman and McLeish[18] for the Rouse time $\tau_e$ of their subchain having $M=14\,470$. Indeed, the relationship between our $\tau$ and their $\tau_e$ is $\tau_e=(1/\pi^2)(M^2/M^2_{\text{subchain}})\tau\cong0.9\times10^{-3}$ s.

Figure 6 refers to the PS390k sample, for which $Z_0$ grows to 54. No adjustable parameter is now available. In particular, since also in this figure $T=130$ °C, both $G$ and $\tau$ remain the same of Fig. 5. The quality of the fit in Fig. 6 is not as good as in the previous case, but it can still be deemed satisfactory. In future work, we will examine in detail possible effects of polydispersity.

### C. Zero-shear viscosity and diffusion coefficient

To confirm the parameter values used so far, specifically the sensitive time constant $\tau$, we further check simulation predictions against data of both zero-shear viscosity and diffusion coefficient. Figure 7 shows the data of zero-shear viscosity for several monodisperse polystyrene melts, as reported by Leonardi *et al.*[19] and Rubinstein and Colby,[16] all reduced to 160 °C. The solid dots in Fig. 7 are simulation results obtained at (nondimensional) shear rates much lower than the (nondimensional) inverse largest relaxation time (see Fig. 3), and made dimensional by using the appropriate parameters which are now fully determined. Thus, we relate $M$ to $Z_0$ through $M=Z_0M_{\text{subchain}}$, while the viscosity requires the product $G\tau$, with $G=0.50$ MPa as given by Eq. (12) and $\tau(160\ ^\circ\text{C})=0.69\times10^{-2}$ s, as obtained from the WLF equation. Figure 7 shows that the solid dots fall on top of data. To further confirm the value of $\tau$, we have also reported as a line in Fig. 7 the prediction for the Rouse viscosity, $\eta_R=(\pi^2/12)(\rho RT/M)\tau_R$ (where $\tau_R=\tau Z_0^2/\pi^2$ is the Rouse relaxation time of the chain), fully agreeing with low-$M$ data.

Figure 8 reports data of center-of-mass diffusion coefficient for several polystyrene melts at 225 °C taken from the review paper of Watanabe,[20] together with our simulation results (solid dots). Our predictions for the diffusion coefficient are obtained by multiplying the nondimensional values in Fig. 3 to the dimensional ratio $a^2/\tau=n_0b^2/\tau$, where

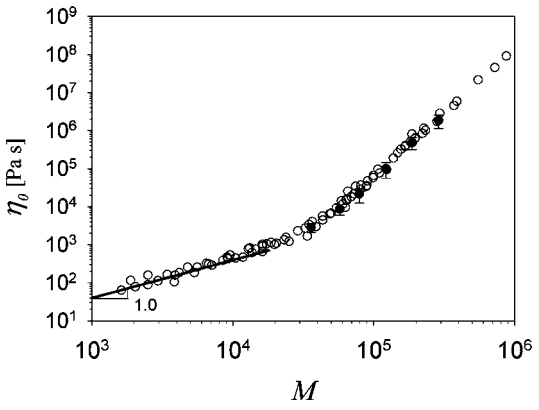


FIG. 7. Zero-shear viscosity of several PS melts at 160 °C as a function of molar mass. The empty circles are data from Refs. 16 and 19 and the solid circles are simulation results. The line for small $M$ is Rouse theory with the same monomeric friction as used in the simulations at high $M$.

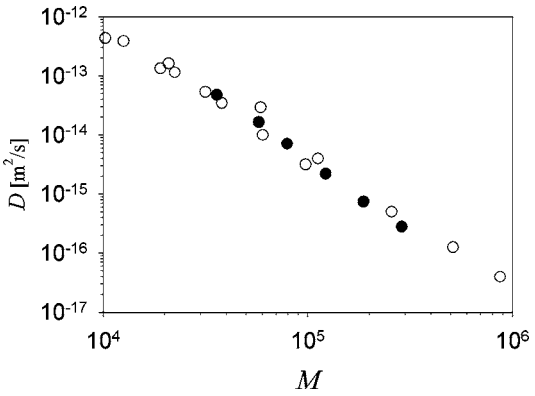


FIG. 8. Center-of-mass diffusion coefficient at 225 °C as a function of $M$. The empty circles are data reported in Ref. 20 and the solid circles are simulation results (with error bars smaller than symbol size).

$\tau(225\ ^\circ\mathrm{C})=2.4\times10^{-5}$ s, $n_0=M_{\mathrm{subchain}}/M_{\mathrm{Kuhn}}=10$ (with $M_{\mathrm{Kuhn}}=720$), and $b=1.8$ nm.[16] Once again, the excellent agreement is taken as a confirmation for the $\tau$ parameter.

### D. Nonlinear behavior

For the nonlinear behavior in shear, we consider the data of Schweizer *et al.*[5] for PS200k-S at 175 °C. Hence, the parameters to be used for the simulations are $Z_0=28$, $G=0.51$ MPa, and $\tau=1.2\times10^{-3}$ s. Since large values of deformation are required to reach steady state in order to avoid that the deformed box becomes too thin, a noncubic box is used, with dimensions of $64\times8\times8$; the box size 64 is along the flow direction.

Figure 9(a) compares data of transient shear viscosity[5] to the simulation results. Large fluctuations in the simulations are observed at low shear rates due to the fact that also the anisotropy (and consequently the stress) are correspondingly very low, and thermal fluctuations dominate. Simulations quantitatively reproduce the transient overshoot behavior at higher shear rates, while discrepancies at short times are seemingly due to inaccuracy of data since the initial slope, required to be unity in a log-log plot, is in the data quite different from unity. The steady-state values of the viscosity emerging from Fig. 9(a) are reported in Fig. 9(b) for both data and simulation. Fluctuating simulation results at low shear rates are averaged over time (at long times) to generate the steady values reported in Fig. 9(b). Good agreement between simulation and data is confirmed. Notice that these comparisons are totally free of adjustable parameters.

In Fig. 9(c), we report the chain stretch λ calculated in our simulations as the ratio of current chain contour length to the equilibrium value. Figure 9(c) shows how chains stretch during startup, showing a maximum in $\langle\lambda\rangle$ that, for the highest shear rates, roughly correlates to the stress overshoot. No stretch emerges at shear rates lower than $\dot\gamma=3$ s$^{-1}$, indicating that the stress overshoots observed in Fig. 9(a) at lower shear rates are due to orientation only. At higher shear rates, both orientation and stretch concur to the overshoot. Such behavior was examined theoretically long ago by Pearson *et al.*[21]

On the quantitative side, it is worth noting that both experiments and simulations show that at smaller shear rates ($\dot\gamma=3$ s$^{-1}$) the deformation $\gamma_{\max}$ at the overshoot is $\gamma_{\max}\cong2.0$, in agreement with the Doi–Edwards theory without chain stretch,[1] while for $\dot\gamma=10$ s$^{-1}$ and $\dot\gamma=30$ s$^{-1}$, significantly larger values are found, i.e., 2.2 and 2.3, from data and simulations, respectively, in the former case and 3.1 and 2.7 in the latter case. Since the chain Rouse time is readily estimated as $\tau_R\cong0.1$ s, agreement with Fig. 3 of Pearson *et al.*[21] is also quantitative. It is worth emphasizing that, as shown in Fig. 9(c), the values of stretch are small and yet they significantly affect the overshoot location. In fact, the smallness of λ allowed us to ignore non-Gaussian effects in shear flows.

Finally, in Fig. 9(d), we report the shear-induced "disen-

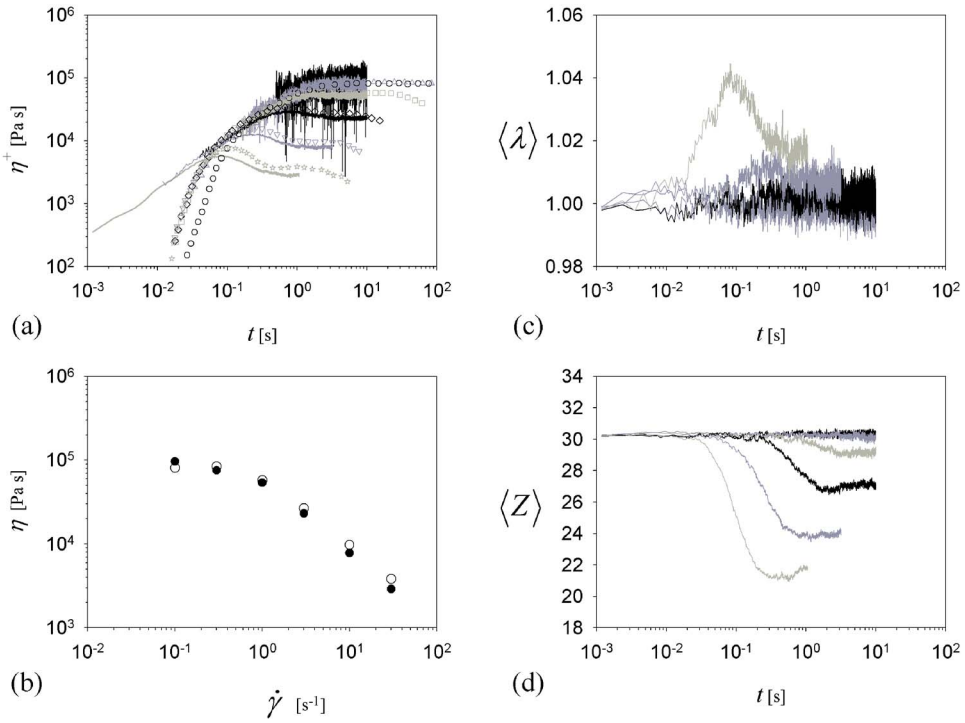


FIG. 9. (Color online) Startup of shear flows for PS200k-S at 175 °C (Ref. 5). Shear rates are $\dot\gamma=0.1$, 0.3, 1, 3, 10, and 30 s$^{-1}$. (a) Viscosity growth as a function of time; here, the symbols are data and the lines are simulations. (b) Steady-state values of viscosity from (a) vs the shear rate. The empty symbols are data and the solid symbols are simulations. (c) Simulation predictions of chain stretch as a function of time. The curve with a pronounced maximum at $t=0.1$ s corresponds to the largest shear rate ($\dot\gamma=30$ s$^{-1}$). (d) Simulation predictions of the mean number of subchains as a function of time and shear rate.

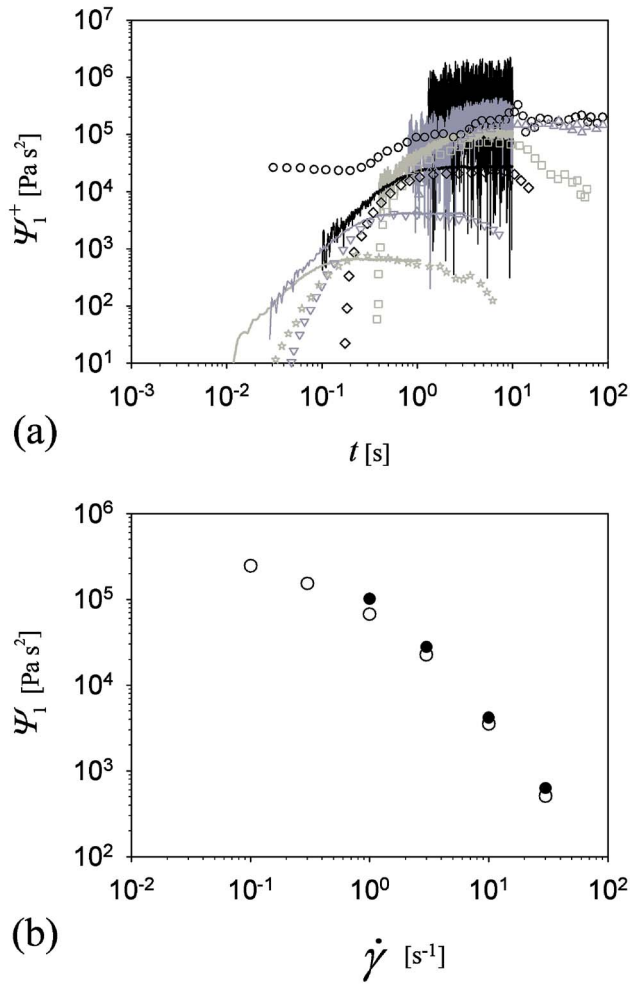


FIG. 10. (Color online) First normal stress difference in startup of shear flows from the same experiments (Ref. 5) and simulations of Fig. 9. (a) Normal stress coefficient as a function of time. (b) Steady values vs shear rate. The empty and solid symbols are data and simulations, respectively. As is apparent in (a), the simulation at the lowest shear rates ($\dot{\gamma}$=0.1 and 0.3 s$^{-1}$) are too noisy for the steady value to be determined.

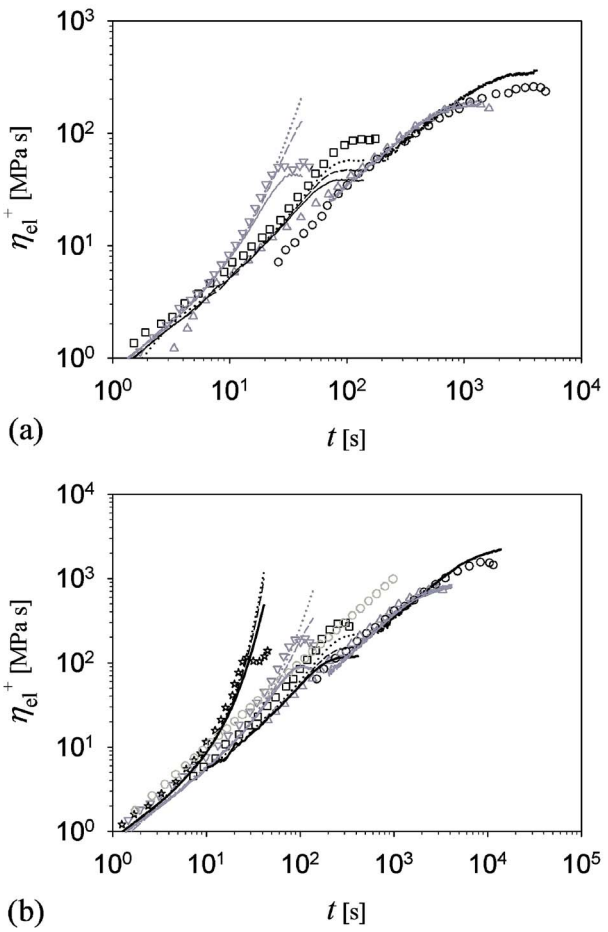


FIG. 11. (Color online) Comparison between Gaussian simulations (lines) and data from Ref. 6 (symbols) for the transient uniaxial extensional viscosity. The dotted, dashed, and full lines correspond to $\Delta t/\tau$=0.01, 0.005, and 0.001, respectively. (a) PS200k at 130 °C. Extension rates are $\dot{\varepsilon}$=0.001, 0.003, 0.03, and 0.1 s$^{-1}$ from right to left. (b) PS390k at 130 °C. Extension rates are $\dot{\varepsilon}$=0.0003, 0.001, 0.01, 0.03, and 0.1 s$^{-1}$ from right to left.

tanglement," as revealed by simulations, in terms of $\langle Z \rangle$ as a function of time. The effect is clearly significant, reaching as much as a 30% reduction in the entanglement number at the largest shear rate ($\dot{\gamma}$=30 s$^{-1}$).

Figure 10(a) compares the transient normal stress coefficient of the same sample considered in Fig. 9 (Ref. 5) with simulation predictions. In Fig. 10(a), at low shear rates, even larger fluctuations are observed than in Fig. 9(a). Here again, short time experimental data seem defective, as a slope of 2 should be observed. Steady-state values are compared with data in Fig. 10(b). Here, the two lowest shear rate simulation results are not reported because of poor statistics, but agreement in the nonlinear range is very good.

Moving on to extensional flows, the aim was to attempt comparison with the uniaxial data of Bach *et al.*[6] Those data were obtained with PS200k and PS390k, both at 130 °C. Hence, simulations are run with $Z_0$=28 and $Z_0$=54, respectively, while comparison with data require the shift factors $G$=0.47 MPa and $\tau$=1.3 s. Also in this case, a noncubic box was used to account for large deformations. The box starts with dimensions of $8\times32\times32$, where 8 is along the stretching direction. The simulation is stopped when the constant-volume deformed box becomes $512\times4\times4$. In view of the chain size and of the periodic boundary conditions, we deemed that 8 is the smallest acceptable dimension at equilibrium, whereas we can perhaps go down to 4 in the lateral directions when chains are longitudinally oriented.

We first consider simulation runs without the non-Gaussian correction. Figures 11(a) and 11(b) show the viscosity growth function under uniaxial extensional flows for the PS200k and PS390k samples, respectively, at various elongational rates $\dot{\varepsilon}$. The simulations reasonably reproduce experimental data at low extension rates, both during the transient and at steady state. At higher $\dot{\varepsilon}$, corresponding to $\dot{\varepsilon}\tau_R > 1$ (see below for an estimate of $\tau_R$), the simulations correctly predict the initial strain hardening shown by the data, but they strongly misbehave at longer times. Indeed, in Fig. 11(a), results for the two highest elongation rates strongly depend on the time step of the integration, as shown by the three curves for each $\dot{\varepsilon}$ value obtained with (from top to bottom) $\Delta t/\tau$=0.01, 0.005, and 0.001, respectively. For the highest $\dot{\varepsilon}$ ($\dot{\varepsilon}\tau_R \approx 10$), the change with $\Delta t$ is even qualitative since, while the highest curve ($\Delta t/\tau$=0.01) shows the expected large Deborah number divergence, the lowest one

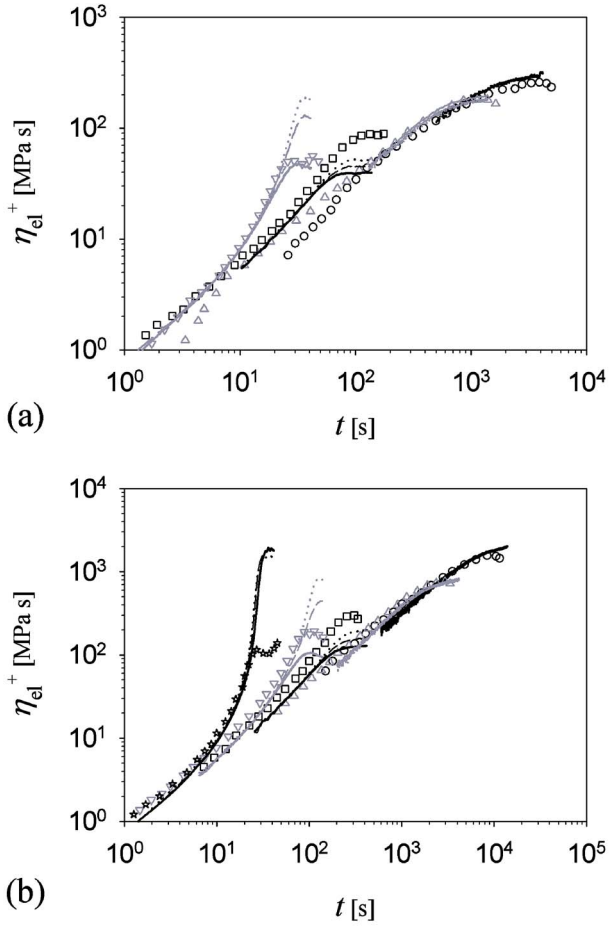


FIG. 12. (Color online) Comparison between non-Gaussian simulations (lines) and data (symbols) for the transient uniaxial extensional viscosity. Lines in (a) and (b) as in Fig. 11.

$(\Delta t/\tau=0.001)$ indicates a possible steady state, which is physically implausible. It looks as if, by decreasing $\Delta t$, the chain relaxes the stretch too soon, corresponding to an effective Rouse time smaller than the real one. The anomalous effect is confirmed in Fig. 11(b), where the three curves for $\dot{\varepsilon}=0.03\ \mathrm{s}^{-1}$ $(\dot{\varepsilon}\tau_R\approx 10)$ are different, with the lowest one even showing a maximum. At the highest rate $(\dot{\varepsilon}=0.1\ \mathrm{s}^{-1},\ \dot{\varepsilon}\tau_R \approx 30)$, however, the expected divergence for the Gaussian chains is recovered for all three values of $\Delta t$.

The unexpected acceleration of stretch relaxation observed at smaller $\Delta t$ might be due to some inconsistency between the dynamical equations and the adopted coarse graining of the model. We are currently investigating on such possibility. It is worth mentioning that the anomaly is restricted to the elongational simulations only. Indeed, for all other results here reported, we have checked time step sensitivity without observing any effect. Finally, it is worth noting that anomalies for the elongational case have been recently found also by Schieber *et al.*[9] by using their CUBS algorithm based on a similar physics.

Concerning the onset of strain hardening as mentioned above, our simulations are in agreement with data and obey the classical criterion $\dot{\varepsilon}_{\mathrm{onset}}\cong\tau_R^{-1}$. Indeed, we obtain $\tau_R(\mathrm{PS200k})=103$ s and $\tau_R(\mathrm{PS390k})=384$ s at 130 °C. We then predict that strain hardening should occur at extensional

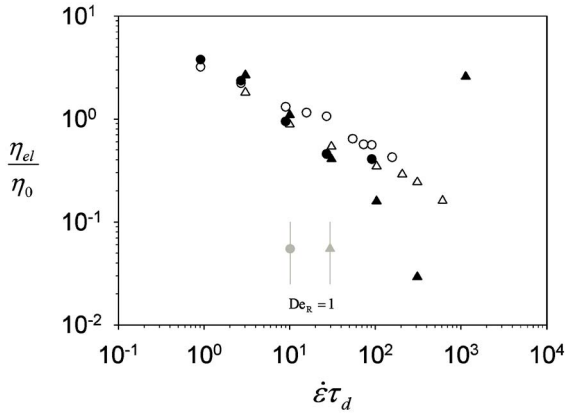


FIG. 13. (Color online) Steady-state extensional viscosity from the results in Fig. 12 (extrapolated to $\Delta t=0$), normalized to the respective zero-shear viscosity (Trouton ratio) vs $\dot{\varepsilon}\tau_d$. The open circles and open triangles are data for PS200k and PS390k, respectively. The closed symbols are the corresponding simulation results. Values used for the zero-shear viscosity and for the disengagement time $\tau_d$ were taken from Ref. 6 as $\eta_0=84$ MPa and $\tau_d=1040$ s for PS200k and $\eta_0=760$ MPa and $\tau_d=11300$ s for PS390k. The vertical segments with circle and triangle mark $De_R=\dot{\varepsilon}\tau_R=1$ for PS200k and PS390k samples, respectively.

rates larger than 0.0097 and 0.0026 $\mathrm{s}^{-1}$ for PS200k and PS390k, respectively, as indeed shown in Fig. 11.

As previously mentioned, non-Gaussian effects in the subchain elastic force are introduced through the function $f(r)$ of Eq. (4). The subchain maximum extension $r_{\max}$ appearing in such equation is (in nondimensional normalized form) $\tilde{r}_{\max}=\tilde{n}\sqrt{n_0}$, with $n_0=10$ in our case. Details on the primitive chain network model accounting for finite extensibility of the polymer chains will be discussed elsewhere. Figure 12 reports the results we obtain with the non-Gaussian code. Also, in this case, the sensitivity on $\Delta t$ remains the only difference being that a steady state is reached in all cases, as indeed expected when finite extensibility is accounted for.

For the non-Gaussian case, the steady-state values obtained at several $\Delta t$ were extrapolated to $\Delta t=0$ so as to obtain the "correct" value (yet subjected to the conceptual uncertainty mentioned previously). Such values of the steady-state viscosities are plotted in Fig. 13 in the form of Trouton ratio versus $\dot{\varepsilon}\tau_d$ by using the zero-shear viscosities and the longest relaxation times as reported by Bach *et al.*[6] for both data and simulations. In the same figure, the vertical bars at $\dot{\varepsilon}\tau_d\approx 10$ and at $\dot{\varepsilon}\tau_d\approx 30$ mark $\mathrm{De}_R=\dot{\varepsilon}\tau_R=1$ for PS200k and PS390k, respectively. Simulations indicate a possible upturn at $\mathrm{De}_R\approx 10$ for both polymers. Significant deviations between simulation predictions and data are found starting at $\mathrm{De}_R\approx 1$.

## IV. CONCLUSIONS

In this paper, we have reported on some modifications of the primitive chain network model which refine the previous version[1,12,22,23] in various respects and also account for finite extensibility in the nonlinear response in fast flows. The results obtained are as follows.

The static chain properties, such as the square end-to-end distance and square radius of gyration, agree with Gauss-

ian chain theory. Similarly, Gaussian are the subchains connecting consecutive sliplinks. The longest relaxation time and the self-diffusion coefficient are compared to the predictions of reptation theory, showing the expected deviations, due to fluctuations, in both absolute values and molar mass scaling.

The experimental $G'$ and $G''$ curves of nearly monodisperse linear polystyrene melts with different molecular weights are quantitatively reproduced with reasonable accuracy by using as single adjustable parameter a basic relaxation time $\tau$ related to the adopted coarse graining. The value of such a parameter is not really adjustable, however, since we could have derived $\tau$ from zero-shear viscosity data of monodisperse melts in the Rouse unentangled regime. Indeed, we have successfully verified that our $\tau$ is quantitatively consistent with such data, and have further confirmed its value against data of both zero-shear viscosity and diffusion coefficient of monodisperse entangled polystyrene melts.

No other parameters being needed, our model can be directly checked against the nonlinear behavior of polystyrene melts. In startup of shear flows, we find quantitative agreement for both the viscosity and first normal stress coefficient growth functions. Also transient elongational viscosities are reasonably reproduced, up to extensional rates of the order of the reciprocal Rouse time. At higher rates, however, only the initial strain hardening is correctly captured. Indeed, at longer times, an unexpected sensitivity to the time step of the integration appears, which in extreme cases even induces changes from a divergent to a steady-state behavior. When this occurs, chain stretch comes out very small, and Gaussian and non-Gaussian simulations virtually coincide. Coincidence of Gaussian and non-Gaussian predictions at high Deborah numbers was also reported in Ref. 9.

In conclusion, the simulation model appears adequate to portray the rheological behavior of entangled systems both in the linear and nonlinear range up to moderate chain stretch. In particular, it is worth emphasizing that literature data on plateau modulus of entangled melts and on viscosity in the Rouse regime *a priori* determine the parameters of the model. The possible inadequacies of the model when chains are expected to become strongly stretched are being investigated.

## ACKNOWLEDGMENTS

We are grateful to Dr. T. Schweizer for providing us with the viscoelastic data on PS200k-S. One of the authors (T.Y.) wishes to thank all members of the Dipartimento di Ingegneria Chimica in Federico II University for their support during his stay there. Mitsui Chemicals, Inc. is thanked for the permission to publish this work. We are also indebted to the anonymous referee for several useful comments, including the suggestion of a careful check on the influence of the integration time step.

[1] M. Doi and S. F. Edwards, *The Theory of Polymer Dynamics* (Clarendon, Oxford, 1986).
[2] C. C. Hua and J. D. Schieber, J. Chem. Phys. **109**, 10018 (1998).
[3] J.-I. Takimoto and M. Doi, Philos. Trans. R. Soc. London, Ser. A **361**, 641 (2003).
[4] Y. Masubuchi, J.-I. Takimoto, K. Koyama, G. Ianniruberto, F. Greco, and G. Marrucci, J. Chem. Phys. **115**, 4387 (2001).
[5] T. Schweizer, J. van Meerveld, and H. C. Ottinger, J. Rheol. **48**, 1345 (2004).
[6] A. Bach, K. Almdal, H. K. Rasmussen, and O. Hassager, Macromolecules **36**, 5174 (2003).
[7] A. Cohen, Rheol. Acta **30**, 270 (1991).
[8] D. M. Nair and J. D. Schieber, Macromolecules **39**, 3386 (2006).
[9] J. D. Schieber, D. M. Nair, and T. Kitkrailard, J. Rheol. **51**, 1111 (2007).
[10] J. D. Ferry, *Viscoelastic Properties of Polymers*, 3rd ed. (Wiley, New York, 1980).
[11] H. M. James and E. Guth, J. Chem. Phys. **11**, 455 (1943).
[12] Y. Masubuchi, G. Ianniruberto, F. Greco, and G. Marrucci, J. Chem. Phys. **119**, 6925 (2003).
[13] K. Kamio, K. Moorthi, and D. N. Theodorou, Macromolecules **40**, 710 (2007).
[14] S. T. Milner and T. C. B. McLeish, Phys. Rev. Lett. **81**, 725 (1998).
[15] T. P. Lodge, Phys. Rev. Lett. **83**, 3218 (1999).
[16] M. Rubinstein and R. H. Colby, *Polymer Physics* (Oxford University Press, Oxford, 2003).
[17] A. Quach and R. Simha, J. Appl. Phys. **42**, 4592 (1971).
[18] A. E. Likhtman and T. C. B. McLeish, Macromolecules **35**, 6332 (2002).
[19] F. Leonardi, J. C. Majesté, A. Allal, and G. Marin, J. Rheol. **44**, 675 (2000).
[20] H. Watanabe, Prog. Polym. Sci. **24**, 1253 (1999).
[21] D. Pearson, E. Herbolzheiner, N. Grizzuti, and G. Marrucci, J. Polym. Sci., Part B: Polym. Phys. **29**, 1589 (1991).
[22] K. Furuichi, C. Nonomura, Y. Masubuchi, G. Ianniruberto, F. Greco, and G. Marrucci, J. Soc. Rheol., Jpn. (Nihon Reoroji Gakkaishi) **35**, 73 (2007).
[23] Y. Masubuchi, G. Ianniruberto, F. Greco, and G. Marrucci, J. Non-Newtonian Fluid Mech. **149**, 87 (2008).